A dedicated compression device for high resolution X-ray tomography of compressed gas diffusion layers

C. Tötzke,[1,2] I. Manke,[1] G. Gaiselmann,[3] J. Bohner,[4] B. R. Müller,[5] A. Kupsch,[5] M. P. Hentschel,[5] V. Schmidt,[3] J. Banhart,[1] and W. Lehnert[4,6]
[1]*Helmholtz-Zentrum Berlin für Materialien und Energie GmbH, 14109 Berlin, Germany*
[2]*Universität Potsdam, 14476 Potsdam, Germany*
[3]*Universität Ulm, 89069 Ulm, Germany*
[4]*Forschungszentrum Jülich, 52425 Jülich, Germany*
[5]*BAM Bundesanstalt für Materialforschung und -Prüfung, 12200 Berlin, Germany*
[6]*RTWH Aachen University, 52062 Aachen, Germany*

(Received 20 February 2015; accepted 5 April 2015; published online 16 April 2015)

We present an experimental approach to study the three-dimensional microstructure of gas diffusion layer (GDL) materials under realistic compression conditions. A dedicated compression device was designed that allows for synchrotron-tomographic investigation of circular samples under well-defined compression conditions. The tomographic data provide the experimental basis for stochastic modeling of nonwoven GDL materials. A plain compression tool is used to study the fiber courses in the material at different compression stages. Transport relevant geometrical parameters, such as porosity, pore size, and tortuosity distributions, are exemplarily evaluated for a GDL sample in the uncompressed state and for a compression of 30 vol.%. To mimic the geometry of the flow-field, we employed a compression punch with an integrated channel-rib-profile. It turned out that the GDL material is homogeneously compressed under the ribs, however, much less compressed underneath the channel. GDL fibers extend far into the channel volume where they might interfere with the convective gas transport and the removal of liquid water from the cell. [http://dx.doi.org/10.1063/1.4918291]

I. INTRODUCTION

Efficient water management of proton-exchange fuel cells (PEFCs) relies on favorable conditions for water and media transport within the gas diffusion layers (GDLs) and is essential for good performance and durability of these cells. A GDL must allow for concurrent transfer of gaseous reactants from the flow-field channels to the electrodes and effective removal of liquid product water. Furthermore, the membrane must be kept humidified to maintain its proton conductivity.[1–4] Common GDL types consist of porous carbon fiber-based materials with carefully adjusted water transport and storage capacities. The transport mechanism of two-phase flow in porous media was the subject of numerous theoretical[5–9] and experimental[10,11] studies. Especially, neutron and X-ray imaging techniques turned out as powerful tools for the investigation of water in porous materials like GDLs.[8,12–27] As transport properties of GDLs are closely linked with their microstructure, precise knowledge of the three-dimensional morphology is the key to understand the functionality of GDLs.[28–30]

A sophisticated way to optimize materials' design is to detect microstructures with improved physical properties by means of model-based computer experiments. Appropriate stochastic geometry models are required to create virtual 3-D structures. The corresponding transport properties can be evaluated by means of numerical transport simulations in these structures. Systematic parameter modification of a geometry model along with numerical transport simulation can efficiently assist the identification of suitable transport geometries.[31–33]

We performed high resolution synchrotron X-ray measurements on various GDL materials at different degrees of compression aiming at the generation of a broad tomographic data set that can be used for the development and validation of stochastically derived geometry models.[33]

II. EXPERIMENTAL SETUP

A. Imaging conditions

The synchrotron imaging experiments were performed at the tomography station of the BAMline using the synchrotron, which is located at the synchrotron source BESSY II (Helmholtz-Zentrum Berlin/Germany).[34]

Monochromatic X-rays were generated by means of a W-Si multilayer monochromator with an energy resolution of $\Delta E/E = 10^{-2}$. In order to achieve optimal contrast for fibers, the beam energy was adjusted to 15 keV. We employed an optical system consisting of a camera (type pco.4000 manufactured by PCO AG), a lens system, and a Gadox scintillator screen to capture digital images with dimensions of 4008×2672 pixel. The pixel size was 0.876 μm, which corresponds to a physical spatial resolution of about 2 μm rendering a field of view of 3.3×2.2 mm^2. The principal setup is sketched in Figure 1.[35] The sample holder was mounted

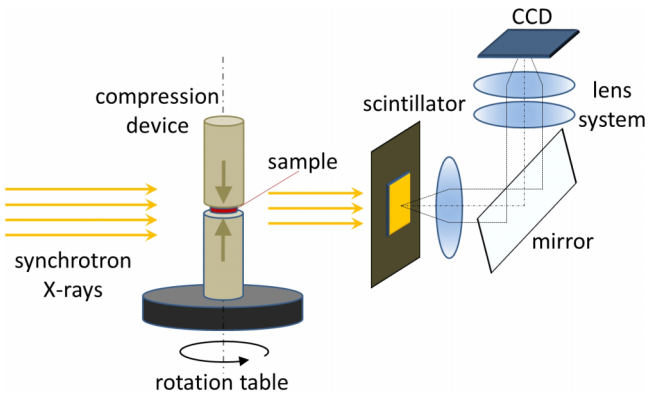

FIG. 1. Scheme of the principal experimental setup at the tomographic instrument.

on a translation/rotation unit. Circular GDL samples with diameters of 3 mm were adjusted. A stepwise rotation over 180° was performed to capture a radiographic set of 1500 projections. In addition, 500 flat-field images were taken to normalize the projections. The exposure time for a single radiograph was 2.5 s plus 1.7 s read-out time referring to a total acquisition time of 140 min for the entire tomographic scan. A flat-field correction of the raw images was performed to remove pixel-to-pixel sensitivity variations of the CCD, horizontal streak artifacts caused by the monochromator and irregularities in the optical pathways such as scratches or dust particle deposited on the scintillator screen or CCD window, respectively, as well as to correct for inhomogeneities of the beam profile. Afterwards, the radiographic dataset was reconstructed to a virtual 3D volume of the sample.

B. Sample compression device

The acquisition of highly resolved synchrotron X-ray absorption tomograms of GDL samples under well-defined compression conditions implies some technically demanding design requirements for the sample holder, i.e., the compression device. Planar and horizontal sample alignment facilitates the data analysis: When aligned in planar, horizontal manner, the sample orientation coincides with the reconstructed tomographic slices what has practical advantages for the geometric analysis. Furthermore, the degree of compression, in terms of the reduction of sample volume, must be precisely adjustable by a compression punch. Therefore, the position of this punch should be controlled with an accuracy of a few micrometers. In order to study different compression patterns, it should be possible to install differently shaped compression punches. A plain punch is sufficient to realize homogeneous compression conditions while a channel profile (see Figure 2(c) right) is required to mimic compression conditions of assembled fuel cells, where the mechanical interaction of GDL and flow-field gives rise for an embossed channel-rib-pattern. Also requirements of the imaging instruments have to be taken into account. The most important points are sufficient beam transmission and dimensional restrictions with regard to the small field of view, which is usually a few millimeters at a resolution of 1 μm. Moreover, the stability of the construction must be appropriate to keep the sample at rest during tomographic scans. Thermal material expansion caused by the energy input of the incident beam should be as small as possible as it could easily influence the sample position within the μm-range.

FIG. 2. Compression device used for high resolution tomography of circular GDL samples. (a) Total view; (b) transparent total view revealing interior details of the construction; (c) sample holder basis (left) and compression punch with integrated channel structure mimicking the flow field channel geometry (right); (d) hollow adjustment screw and sleeve made of brass; and (e) detail of the adjustment screw showing the male ultra-fine thread (pitch = 200 μm).

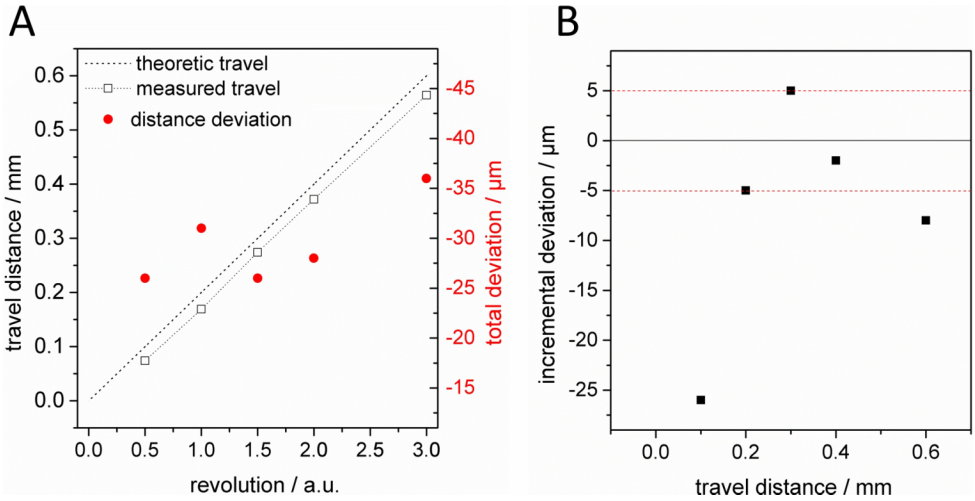

FIG. 3. Positioning accuracy of the compression punch. (a) Travel distance of compression punch plotted as a function of setting screw rotation. Theoretic travel as given by the thread pitch. (b) Incremental deviation for the stepwise travel of the punch. First measure point (at 0.1 mm) reflects the free play of the punch-setting screw connection. Position accuracy of ±5 μm can be achieved for position steps <0.1 mm or 1/2 screw rotation (see text).

A dedicated compression device that can cope with these technical challenges was designed and manufactured by Forschungszentrum Jülich.

Figure 2 illustrates the principal design of the compression device which basically consists of the sample bearing base part (Figure 2(c) left) and the compression unit fastened on top. This unit is built up as follows: a metal sleeve (Figure 2(d) right) with a female ultra-fine thread is screwed into the polyimide casing. The compression punch positioned beneath travels downward when the adjustment screw is fastened (Figure 2(d) left). When unscrewing it, the punch is returned by a retaining spring. A mounting pin guided in a groove of the polyimide casing prevents any rotation of the travelling punch to ensure a torsion-free sample compression.

The design of the compression device facilitates quick and easy exchange of samples, which helps to save valuable beam time at the electron storage ring. After the compression unit has been unfastened, the sample can be mounted on the top plateau of the base part.

Subsequently, the compression unit is refastened and the punch can be settled. As the pitch of the setting screw is 200 μm, a full screw rotation will drive the punch 200 μm downwards. When approaching the sample in smaller steps, it is possible to adjust punch position and, hence, the sample thickness very precisely. For this, the relative position of the punch can be checked with a scale reading while its absolute position is double-checked radiographically by the CCD camera. Figure 3 demonstrates that the punch position can be adjusted with a precision of about ±5 μm when approaching the sample step by step with increments no larger than half of a screw rotation.

The casing of the compression device is made of durable high-performance polyimide-based polymer (Vespel®). Within the field of view, its wall thickness has been reduced to 1 mm to achieve high beam transmission. The compression unit can be assembled with different compression tools: a planar punch to realize a homogeneous compression and a punch with integrated channel profile (0.8 mm wide and 1 mm deep) (see Figure 2(c), right). The maximum possible pressure of the device is limited to about 1-3 MPa, i.e., the device is optimized for soft materials and not suited for hard materials like rocks or metals.[36] A summary of some important parameters of the device can be found in Table I.

III. RESULTS AND DISCUSSION

The present tomographic study covers a range of different GDL materials measured at four stages of increasing compression (0, 10, 20, and 30 vol.%). In this paper, we exemplarily show results for the morphology of the material type H2315 (manufactured by Freudenberg FCCT) in the uncompressed state and compressed by 30% of initial volume. This material represents a standard nonwoven GDL material without water proofing additives or binder. Figure 4 shows half of the reconstructed volume of the same sample in the uncompressed and compressed states. The sample was virtually cut to show a cross section of the material. The initial GDL thickness of about 220 μm is reduced by 30% to a value of 176 μm. The thickness reduction of the sample did not result in a significant lateral expansion, i.e., no significant diameter extension was observed. This suggests that mainly the pore space was compressed. Upon reconstruction, the sample volume was binarized employing a global threshold to separate pore space from the solid phase (fibers).

TABLE I. Some important parameters of the compression device.

Maximum sample diameter	3 mm
Maximum diameter of device	28 mm
Field of view (X-rays)	4.4 mm × 2.9 mm
Precision of compression	±5 μm
Channel profile width/height	0.8 mm/1 mm
Maximum clamping pressure	1-3 MPa
Operating temperature	20-50 °C
Material	Vespel SP-1

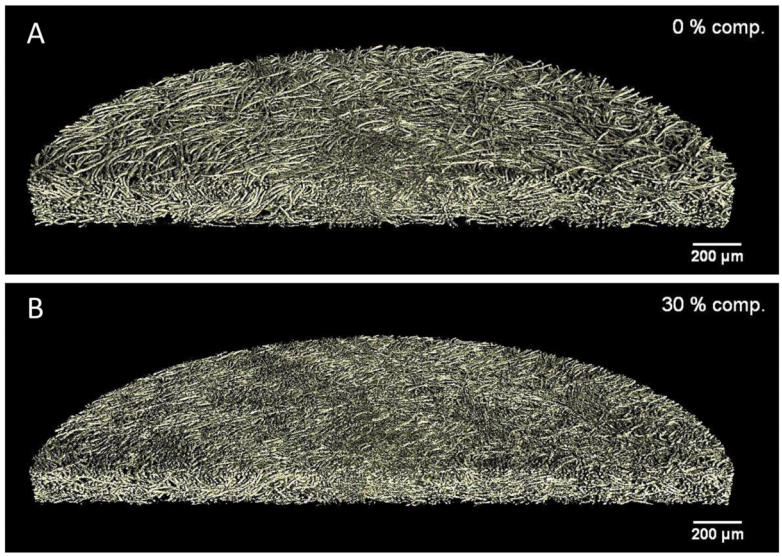

FIG. 4. 3D representation of the (a) uncompressed and (b) compressed GDL samples (by 30 vol.%) (type Freudenberg H2315).

TABLE II. Porosity and mean geometric tortuosity computed for the uncompressed and compressed GDLs.

Compression (vol. %)	Porosity	Mean tortuosity	Standard deviation (tortuosity)
0	0.78	1.50	0.099
30	0.67	1.48	0.092

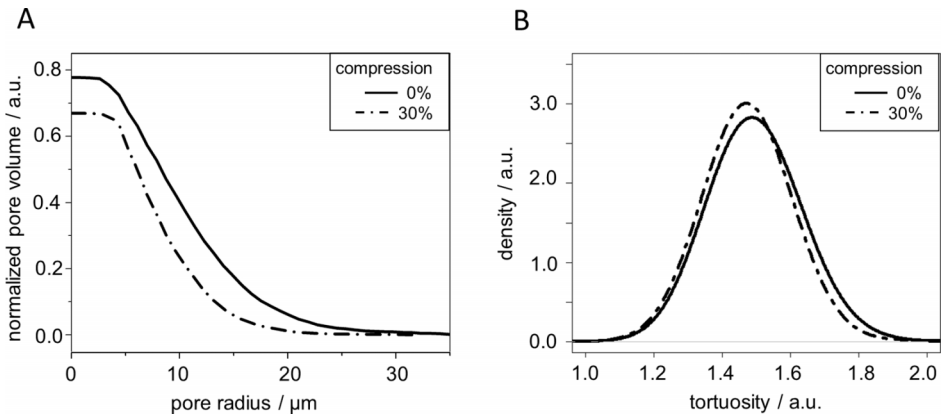

FIG. 5. (a) cPSD and (b) distribution of geometric tortuosity P (right) computed for uncompressed and compressed states.

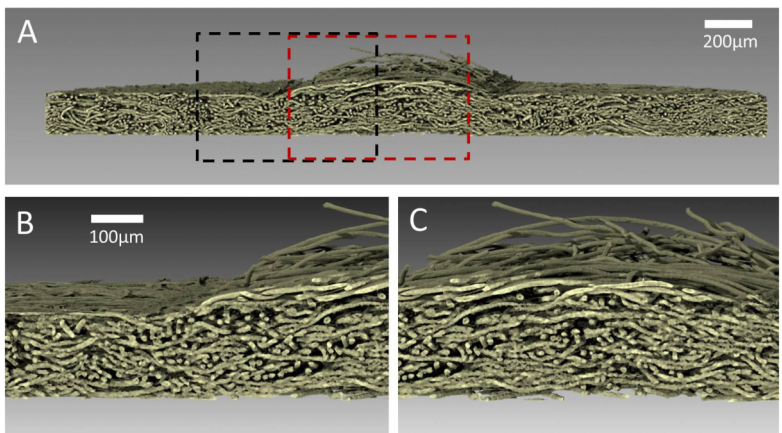

FIG. 6. (a) 3D rendering of a compressed GDL demonstrating the inhomogeneous compression caused by the channel-rib pattern of the flow-field; (b) transition zone between channel and rib areas; and (c) GDL structure underneath the channel.

In order to analyze the influence of compression on the microstructure, several structural characteristics are calculated and compared to each other for uncompressed and 30% compressed GDL, respectively. First, the porosity and the mean geometric tortuosity are stated in Table II.

Subsequently, the spherical contact distribution functions $H: [0,\infty) \rightarrow [0,1]$ from background (pore) to foreground (solid) phase are computed, where H(t) is the probability that the minimum distance from a randomly chosen point of the pore phase to the solid phase is not larger than $t > 0$. As further structural characteristic, the continuous pore size distribution (cPSD) $[0,\infty) \rightarrow [0,1]$ has been calculated for the uncompressed and compressed GDLs, where P(t) is the volume fraction, which can be covered by spheres with center belonging to the pore phase, and radius t, such that these spheres have no intersection with the foreground phase, see Münch and Holzer.[37] The results are displayed in Figure 5(a).

Furthermore, for the porous material considered in the present paper, the geometrical properties of the percolation pathways through the pore phase play an important role for the transport of gas-molecules within the GDL. Therefore, we investigated the "geometric tortuosity" of the pore space, which is defined as the Euclidean length of shortest paths along the edges of a geometric 3D graph representing the possible paths through the pore phase divided by the material thickness in the considered transport direction (perpendicular to the material surface). In other words, this parameter describes the windiness of transport paths through the porous materials. The geometric 3D graph of the pore phase is computed by means of the skeletonization algorithm implemented in software Avizo 7. Note that starting from a randomly chosen location on top of the porous material, its geometric tortuosity can be represented by a probability distribution instead of looking at the mean tortuosity only, see, e.g., Thiedmann *et al.*[38] The results are given in Table II and Figure 5(b). In addition to the demonstrated impact of homogeneous compression on transport-relevant geometric parameter of the GDL microstructure, we have also simulated the effect of inhomogeneous compression caused by the mechanical interaction of the GDL with the channel-rib-pattern of the flow-field. We used the compression tool with the integrated channel profile to simulate the influence of the flow-field geometry to compress the GDL by 30% of its initial thickness. Figure 6 shows a perspective view on the GDL sample that was compressed. The sample was virtually cut to provide a cross sectional insight. The visualization of the reconstructed volume shows nicely that the shape of the compressing tool is stamped into the GDL sample generating considerable differences in the local material density. While the GDL under the ribs is homogeneously compressed to the thickness determined by the compression tool, the GDL fiber structure is much less compressed below the channel. Along the center line of the channel, the GDL thickness almost remains unaltered. Consequently, when assembled in fuel cells, the GDL material significantly extends into the channel volume where it exerts influence on the media flow. Figure 6 also documents that some individual fiber endings are erected by the bending stress exerted by the channel edge. This fiber end may have a significant influence on the gas flow profile inside the channel and could alter the flow regime, e.g., by producing vortexes.

Figures 6(b) and 6(c) show that the characterization of the microstructure in terms of the transport relevant geometric parameters requires a partition in sub-areas according to the relative position with respect to the channel-rib-pattern of the flow-field. While the areas underneath ribs can be handled equivalently to the case of a homogeneously compressed GDL, the local geometric parameters within the transition zone along the channel edges vary strongly (see Figure 6(b)).

IV. CONCLUSION AND OUTLOOK

Synchrotron X-ray tomography was demonstrated to be a powerful tool to analyze the microstructure of porous fiber-based materials such as nonwoven GDL. Taking advantage of dedicated compression device, highly resolved tomographic data of compressed GDL morphologies can be produced.[33] These data are used for geometric analysis of transport relevant structure parameter and serve as experimental basis to develop mathematical structure models.[32] This approach paves the way for virtual material design, i.e., the generation of virtual GDL structures with optimized physical properties.

ACKNOWLEDGMENTS

We gratefully acknowledge funding of the research by the German Federal Ministry for Education and Science (BMBF) under Grant Nos. 05M10KTA, 05M10CJA, 05M10VUA, and 05M10DAA.

[1]C.-Y. Wang, Chem. Rev. **104**(10), 4727-4766 (2004).
[2]*Handbook of Fuel Cells–Fundamentals Technology and Applications*, edited by W. Vielstich, A. Lamm, and H. A. Gasteiger (John Wiley & Sons, Chichester, 2003), Vol. 3.
[3]L. Carrette, K. A. Friedrich, and U. Stimming, Fuel Cells **1**(1), 5-39 (2001).
[4]J. R. Bunn, D. Penumadu, R. Woracek, N. Kardjilov, A. Hilger, I. Manke, and S. Williams, Appl. Phys. Lett. **102**(23), 234102 (2013).
[5]U. Pasaogullari and C.-Y. Wang, J. Electrochem. Soc. **152**(2), A380-A390 (2005).
[6]C. Ziegler, H. M. Yu, and J. O. Schumacher, J. Electrochem. Soc. **152**(8), A1555-A1567 (2005).
[7]C. Y. Wang and P. Cheng, Int. J. Heat Mass Transfer **39**(17), 3607-3618 (1996).
[8]P. K. Sinha, P. P. Mukherjee, and C. Y. Wang, J. Mater. Chem. **17**, 3089-3103 (2007).
[9]P. Zhou and C. W. Wu, J. Power Sources **195**, 1408-1415 (2010).
[10]A. Bazylak, D. Sinton, and N. Djilali, J. Power Sources **176**(1), 240-246 (2008).
[11]S. Litster, D. Sinton, and N. Djilali, J. Power Sources **154**(1), 95-105 (2006).
[12]R. J. Bellows, M. Y. Lin, M. Arif, A. K. Thompson, and D. Jacobson, J. Electrochem. Soc. **146**(3), 1099-1103 (1999).
[13]R. Satija, D. L. Jacobson, M. Arif, and S. A. Werner, J. Power Sources **129**(2), 238-245 (2004).
[14]M. A. Hickner, N. P. Siegel, K. S. Chen, D. S. Hussey, D. L. Jacobson, and M. Arif, J. Electrochem. Soc. **155**(4), B427-B434 (2008).
[15]A. B. Geiger, A. Tsukada, E. Lehmann, P. Vontobel, A. Wokaun, and G. G. Scherer, Fuel Cells **2**(2), 92-98 (2002).
[16]P. Boillat, G. Frei, E. H. Lehmann, G. G. Scherer, and A. Wokaun, Electrochem. Solid-State Lett. **13**(3), B25-B27 (2010).
[17]N. Pekula, K. Heller, P. A. Chuang, A. Turhan, M. M. Mench, J. S. Brenizer, and K. Ünlü, Nucl. Instrum. Methods Phys. Res., Sect. A **542**(1-3), 134-141 (2005).

[18]P. K. Sinha, P. Halleck, and C.-Y. Wang, Electrochem. Solid-State Lett. **9**(7), A344-A348 (2006).
[19]I. Manke, C. Hartnig, M. Grünerbel, W. Lehnert, N. Kardjilov, A. Haibel, A. Hilger, J. Banhart, and H. Riesemeier, Appl. Phys. Lett. **90**(17), 174105 (2007).
[20]C. Hartnig, I. Manke, J. Schloesser, P. Krüger, R. Kuhn, H. Riesemeier, K. Wippermann, and J. Banhart, Electrochem. Commun. **11**(8), 1559-1562 (2009).
[21]C. Tötzke, I. Manke, A. Hilger, G. Choinka, N. Kardjilov, T. Arlt, H. Markötter, A. Schroder, K. Wippermann, D. Stolten, C. Hartnig, P. Krüger, R. Kuhn, and J. Banhart, J. Power Sources **196**(10), 4631-4637 (2011).
[22]S. R. Stock, Int. Mater. Rev. **53**, 129-181 (2008).
[23]R. Kuhn, J. Scholta, P. Krüger, C. Hartnig, W. Lehnert, T. Arlt, and I. Manke, J. Power Sources **196**(12), 5231-5239 (2011).
[24]W. Maier, T. Arlt, C. Wannek, I. Manke, H. Riesemeier, P. Krüger, J. Scholta, W. Lehnert, J. Banhart, and D. Stolten, Electrochem. Commun. **12**(10), 1436-1438 (2010).
[25]A. Schröder, K. Wippermann, J. Mergel, W. Lehnert, D. Stolten, T. Sanders, T. Baumhöfer, D. U. Sauer, I. Manke, N. Kardjilov, A. Hilger, J. Schloesser, J. Banhart, and C. Hartnig, Electrochem. Commun. **11**(8), 1606-1609 (2009).
[26]A. Lange, A. Kupsch, M. P. Hentschel, I. Manke, N. Kardjilov, T. Arlt, and R. Grothausmann, J. Power Sources **196**(12), 5293-5298 (2010).
[27]H. Markötter, J. Haussmann, R. Alink, C. Tötzke, T. Arlt, M. Klages, H. Riesemeier, J. Scholta, D. Gerteisen, J. Banhart, and I. Manke, Electrochem. Commun. **34**, 22-24 (2013).
[28]H. Markötter, I. Manke, P. Krüger, T. Arlt, J. Haussmann, M. Klages, H. Riesemeier, C. Hartnig, J. Scholta, and J. Banhart, Electrochem. Commun. **13**(9), 1001-1004 (2011).
[29]H. Markötter, R. Alink, J. Haussmann, K. Dittmann, T. Arlt, F. Wieder, C. Tötzke, M. Klages, C. Reiter, H. Riesemeier, J. Scholta, D. Gerteisen, J. Banhart, and I. Manke, Int. J. Hydrogen Energy **37**(9), 7757-7761 (2012).
[30]R. Alink, J. Haußmann, H. Markötter, M. Schwager, I. Manke, and D. Gerteisen, J. Power Sources **233**, 358-368 (2013).
[31]G. Gaiselmann, D. Froning, C. Tötzke, C. Quick, I. Manke, W. Lehnert, and V. Schmidt, Int. J. Hydrogen Energy **38**(20), 8448-8460 (2013).
[32]G. Gaiselmann, C. Tötzke, I. Manke, W. Lehnert, and V. Schmidt, J. Power Sources **257**, 52-64 (2014).
[33]C. Tötzke, G. Gaiselmann, M. Osenberg, J. Bohner, T. Arlt, H. Markötter, A. Hilger, F. Wieder, A. Kupsch, B. R. Müller, M. P. Hentschel, J. Banhart, V. Schmidt, W. Lehnert, and I. Manke, J. Power Sources **253**, 123-131 (2014).
[34]W. Görner, M. P. Hentschel, B. R. Müller, H. Riesemeier, M. Krumrey, G. Ulm, W. Diete, U. Klein, and R. Frahm, Nucl. Instrum. Methods Phys. Res., Sect. A **467-468**(Part 1), 703-706 (2001).
[35]S. H. Williams, A. Hilger, N. Kardjilov, I. Manke, M. Strobl, P. A. Douissard, T. Martin, H. Riesemeier, and J. Banhart, J. Instrum. **7**, P02014 (2012).
[36]S. Zabler, A. Rack, I. Manke, K. Thermann, J. Tiedemann, N. Harthill, and H. Riesemeier, J. Struct. Geol. **30**(7), 876-887 (2008).
[37]B. Münch and L. Holzer, J. Am. Ceram. Soc. **91**(12), 4059-4067 (2008).
[38]R. Thiedmann, C. Hartnig, I. Manke, V. Schmidt, and W. Lehnert, J. Electrochem. Soc. **156**(11), B1339-B1347 (2009).